Observation of Topological Hall Effect in a Chemically Complex Alloy

Jihao Yu, Yuying Liu, Yubin Ke, Jiaqi Su, Jingshan Cao, Zian Li,* Baoan Sun,* Haiyang Bai,* and Weihua Wang

The topological Hall effect (THE) is the transport response of chiral spin textures and thus can serve as a powerful probe for detecting and understanding these unconventional magnetic orders. So far, the THE is only observed in either noncentrosymmetric systems where spin chirality is stabilized by Dzyaloshinskii–Moriya interactions, or triangular-lattice magnets with Ruderman–Kittel–Kasuya–Yosida-type interactions. Here, a pronounced THE is observed in a Fe-Co-Ni-Mn chemically complex alloy with a simple face-centered cubic (fcc) structure across a wide range of temperatures and magnetic fields. The alloy is shown to have a strong magnetic frustration owing to the random occupation of magnetic atoms on the close-packed fcc lattice and the direct Heisenberg exchange interaction among atoms, as evidenced by the appearance of a reentrant spin glass state in the low-temperature regime and the first principles calculations. Consequently, THE is attributed to the nonvanishing spin chirality created by strong spin frustration under the external magnetic field, which is distinct from the mechanism responsible for the skyrmion systems, as well as geometrically frustrated magnets.

J. Yu, J. Cao, B. Sun, H. Bai, W. Wang
Institute of Physics
Chinese Academy of Sciences
Beijing 100190, China
E-mail: sunba@iphy.ac.cn; hybai@iphy.ac.cn
J. Yu, J. Cao, B. Sun, H. Bai, W. Wang
Center of Materials Science and Optoelectronics Engineering
University of Chinese Academy of Sciences
Beijing 100049, China
Y. Liu, J. Su, Z. Li
School of Physical Science and Technology
Guangxi University
Nanning 530004, China
E-mail: zianli@gxu.edu.cn
Y. Ke
Spallation Neutron Source Science Center
Dongguan 523803, China
Y. Ke
Institute of High Energy Physics
Chinese Academy of Sciences
Beijing 100049, China
B. Sun, H. Bai, W. Wang
Songshan Lake Materials Laboratory
Dongguan, Guangdong 523808, China

The ORCID identification number(s) for the author(s) of this article can be found under https://doi.org/10.1002/adma.202308415

DOI: 10.1002/adma.202308415

1. Introduction

When competing spin interactions cannot be satisfied simultaneously within a magnetic material, long-range orders, such as ferromagnetic and antiferromagnetic orders, may be suppressed. In some cases, this can lead to the formation of non-coplanar chiral spin textures (CSTs).[1–5] Their exotic electromagnetic properties have aroused numerous interests both fundamentally, relevant for theoretical research on magnetic monopoles[6] and gauge field[7] theory in condensed matter physics, and practically for the potential information carriers in the next-generation storage and logic devices.[8–10] They are characterized by scalar spin chirality and nontrivial topological properties. When itinerant electrons hop over a CST, they will collect a real-space Berry phase that is proportionate to the solid angle subtended by localized spins in the vicinity.[11,12] This phase generates a fictitious magnetic field detectable via an additional transverse voltage drop, known as the topological Hall effect (THE),[13] which serves as a transport signature of CSTs. Notably, THE plays an essential role in the electrical detection of these textures, especially at smaller scales, such as a few nanometers or smaller.[14–17]

Nanometer-sized CSTs and the accompanying THE have been observed both in bulk noncentrosymmetric lattice structures, like the B20 MnSi compounds;[2,18] and in interfacial symmetry-breaking heterostructures[19–22] such as ultrathin magnetic films epitaxially grown on heavy metals.[23–25] The formation of such spin textures owes to the Dzyaloshinskii–Moriya (DM) interactions that are induced by spin-orbit coupling (SOC) in materials lacking central or inversion symmetry.[26] However, the stabilization of CSTs typically requires either low temperatures or high magnetic fields. Recent theories have proposed an additional mechanism through which spin chirality can be stabilized by magnetic frustration.[27–30] This mechanism has been observed in some geometrically frustrated centrosymmetric structures, such as the hexagonal structure Gd_2PdSi_3, with a triangular lattice of Gd^+ spins.[27] In the centrosymmetric materials, the DM interactions are typically absent or cancel out globally and thus, the Ruderman–Kittel–Kasuya–Yosida (RKKY)-type interaction among local $4f$ moments dictates the properties.[31–33] However, the RKKY interaction is long-range and indirect and often

**ADVANCED
SCIENCE NEWS**

www.advancedsciencenews.com
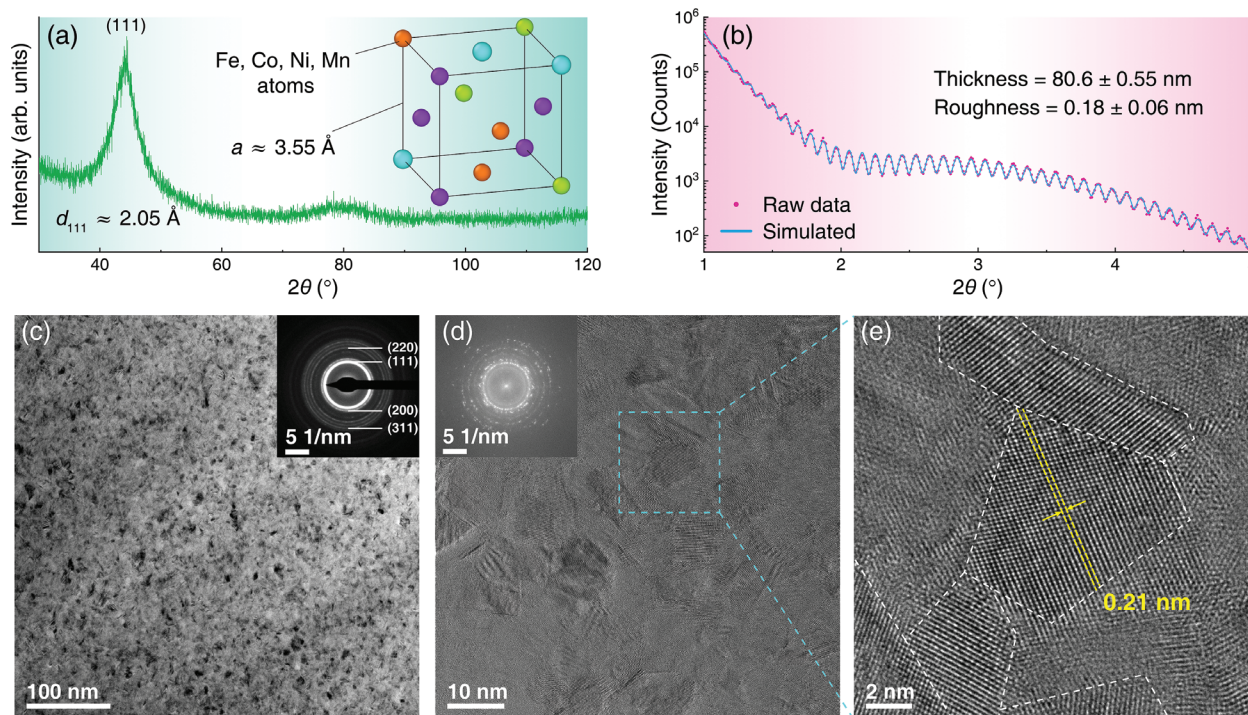
**ADVANCED
MATERIALS**

www.advmat.de

Figure 1. Structural characterizations of the FCNM CCA film H1. a) GI-XRD patterns and the corresponding crystal structure. b) Measured and simulated XRR patterns showing the thickness and the roughness. c) BF-TEM image and SAED pattern (inset) showing the polycrystalline microstructure. d) HR-TEM image and corresponding FFT pattern (inset) showing the nanoscale fcc grains. e) Enlarged view of the region marked in (d) showing the lattice image of a single grain.

yields a relatively weak or moderate magnetic frustration.[34] So far, CSTs in other material systems have not been reported yet. Research into the CSTs and their related exotic topological properties, based on novel physical mechanisms, has become one of the central directions in condensed matter physics.[35,36]

Chemically complex alloys (CCAs) or high entropy alloys are an emerging class of advanced materials composed of multiple principal elements in near equiatomic ratios. Unlike complex intermetallic phases, they typically form single-phase random solid solutions with simple crystal structures.[37–39] Compared to traditional alloys based on one or two major elements, CCAs display novel and diverse properties that cannot be achieved from any of the constituent elements alone.[40,41] Here, we observed a notable THE in a Fe-Co-Ni-Mn CCA film with a simple face-centered cubic (fcc) (centrosymmetric) structure. We attributed the THE to a unique mechanism, that is, the nonvanishing spin chirality formed by the shrinkage of solid angles subtended by localized spins under an external magnetic field owing to the strong magnetic frustration in the alloy system. This is also corroborated by small-angle neutron scattering (SANS) experiments that reveal the spin distribution.

2. Results

2.1. Material Systems and Structural Characterization

Considering that thin films facilitate the precise measurements of transport properties, as well as the device fabrication, we prepared quaternary Fe-Co-Ni-Mn CCA thin films by physical va-

por deposition method as described in the Experimental Section. Two types of FCNM CCA films (designated as H1 and H2) were synthesized using targets with the same composition ($Fe_{25}Ni_{25}Co_{25}Mn_{25}$) but prepared by different methods, that is, induction melting and powder sintering. These films exhibit varying compositions and microstructures. **Figure 1** shows the structural characterization of an H1 sample. The grazing-incident X-ray diffraction (GI-XRD) pattern in Figure 1a shows that only the first Bragg peak of the fcc lattice structure exists, corresponding to the (111) plane. This peak is fairly broad, which could be due to the nanoscale grain size. The lattice parameter, calculated from the peak position, is $a \approx 3.55$ Å. The thickness (t) and the roughness (σ) of the H1 film sample were measured using X-ray reflectivity (XRR) with values of 80.6 and 0.18 nm, respectively (Figure 1b). The other H1 sample has a film thickness of 1.9 μm, as determined by cross-sectional scanning electron microscopy (SEM) analysis (Figure S1, Supporting Information). The bright-field (BF) transmission electron microscopy (TEM) image of the H1 sample (Figure 1c) reveals a single-phase nanocrystalline structure. The nanocrystals exhibit typical polycrystalline rings that correspond to the fcc structure, as verified by the selected-area electron diffraction (SAED) patterns (inset of Figure 1c). The fcc structure of the H1 sample is further corroborated by the high-resolution TEM (HR-TEM) image (Figure 1d), and its corresponding fast-Fourier transformation (FFT, inset of Figure 1d). The magnified HR-TEM (Figure 1e) indicates that the nanocrystals have an average grain size of about 10 nm. The H2 sample also possesses an fcc structure, but its average grain size (which is no less than 10 μm) is significantly
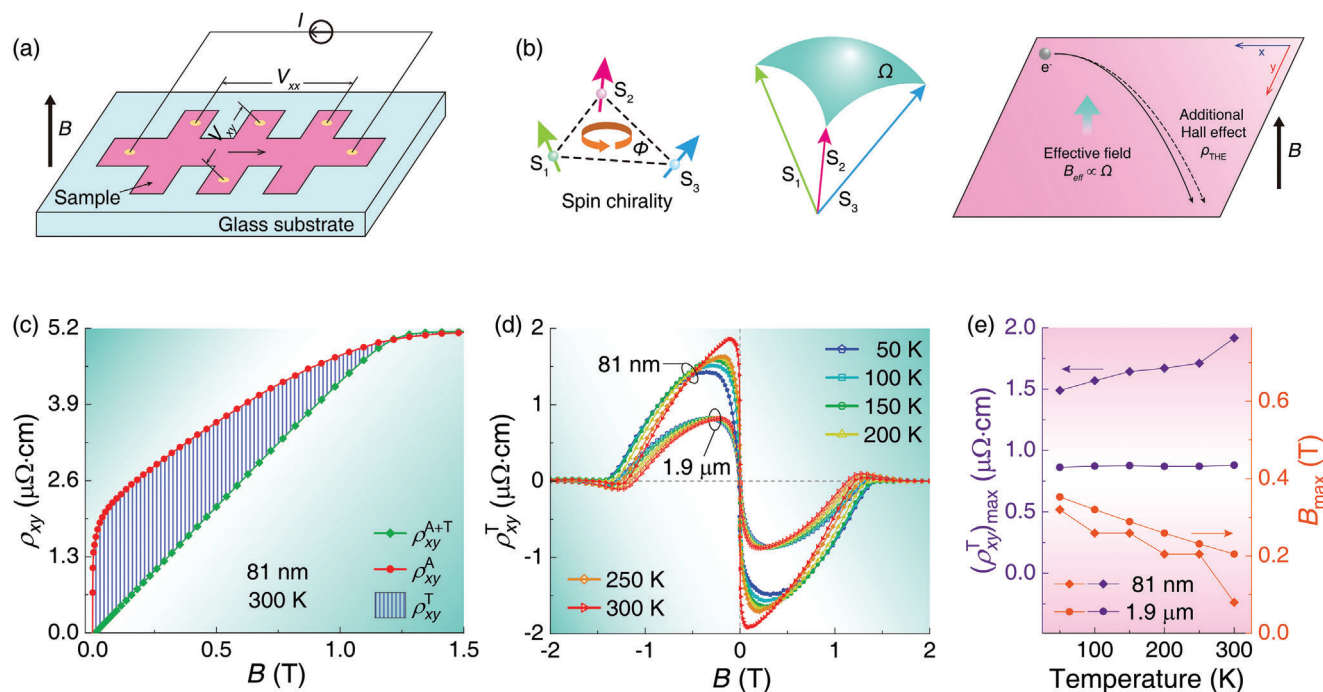
Figure 2. Transport property measurements of the FCNM CCA film. a) Schematic diagram of FCNM CCA film grown on a glass substrate with electric contacts. b) Schematics of the underlying mechanism of THE. c) Topological Hall signals (shaded area) acquired from transport (green curve) and magnetic (red curve) property measurements for the 81-nm H1 sample at $T = 300$ K. d) Intensity of THE for the H1 samples at various temperatures. e) Amplitude and peak position of THE versus temperature for the H1 samples.

larger than that of H1 (Figure S2, Supporting Information). The compositions of H1 and H2, as determined by SEM energy-dispersive X-ray spectroscopy (EDS), are $Fe_{37}Co_{24}Ni_{22}Mn_{17}$ and $Fe_{22}Co_{30}Ni_{35}Mn_{13}$, respectively (at atomic percentage). Moreover, EDS mappings demonstrate that the distributions of principal elements (Fe, Co, Ni, and Mn) in the H1 and H2 samples are homogeneous (Figure S3, Supporting Information), with no composition segregation at the nanoscale. FCNM bulk CCAs are known to exhibit a propensity for forming a random solid solution.[38] As evidenced by the results above, this behavior also extends to the FCNM CCA films (the inset of Figure 1a).

2.2. Topological Hall Effects

For the transport measurements, the CCA films were grown on glass substrates using a stainless-steel mask in the Hall-bar shape, as illustrated in **Figure 2a**. Platinum wires with silver paste were used to make the electric contacts. Typically, the transverse resistivity of a magnetic metal can be divided into three components

$$\rho_{xy} = \rho_{xy}^{O} + \rho_{xy}^{A} + \rho_{xy}^{T} \qquad (1)$$

The first two terms ρ_{xy}^{O} and ρ_{xy}^{A} correspond to the ordinary Hall effect (OHE) and the anomalous Hall effect (AHE), which are proportional to the applied magnetic field B and the spontaneous magnetization M, respectively. The THE term ρ_{xy}^{T} is caused by the scalar spin chirality defined by $\chi_{123} = S_1 \cdot (S_2 \times S_3)$, where $S_i = (S_i^x, S_i^y, S_i^z)(i = 1, 2, 3)$ represent spin vectors on neighboring

sites (Figure 2b). Note that the expression of χ_{123} also equals the solid angle subtended by S_i. When hopping over a CST, the electron acquires a geometric phase proportional to χ_{123}, which creates an additional magnetic flux. Take the H1 (81 nm) sample at 300 K as an example, the contribution of THE can be extracted by removing the OHE and the AHE parts, which is the common approach for most systems with THE.[35] For the OHE component, we have $\rho_{xy}^{O} = R_0 B$ where R_0 is the ordinary Hall coefficient. Therefore, it can be acquired by the linear fitting to the high-field part of the raw Hall signal. Then the sum of the AHE and the THE components is given by $\rho_{xy}^{A+T} = \rho_{xy} - \rho_{xy}^{O}$ (the green curve in Figure 2c). From the empirical relation of AHE, we have $\rho_{xy}^{A} = R_s M$, where R_s is the anomalous Hall coefficient. Since CSTs are suppressed at the saturated field, ρ_{xy}^{A} can be inferred by scaling the magnetic hysteresis loop to the ρ_{xy}^{A+T} curve at the maximum field where ρ_{xy}^{T} is considered to be zero (the red curve in Figure 2c). Here we use a simplified method to extract the AHE because the magnetoresistance (MR) of the FCNM CCA films is quite small, that is, <0.1% and <0.04% for H1 and H2 samples, respectively (Figure S4, Supporting Information). So the analysis of AHE can be simplified.[42]

Figure 2d shows the measured THE intensity ρ_{xy}^{T} for two H1 samples with different thicknesses at varying temperatures. As can be seen, all curves exhibit the same trend. THE can be observed across a wide temperature range (at least from 50 to 300 K in our case) and can withstand an external field of up to 1.8 T. THE intensity is weaker for the thicker sample, which may be due to disparities in the demagnetizing factor and the proportion of surface magnetic moments. Figure 2e displays the

**ADVANCED
SCIENCE NEWS**

www.advancedsciencenews.com

**ADVANCED
MATERIALS**

www.advmat.de

maximum THE $(\rho^T_{xy})_{max}$ and its corresponding external field B_{max} versus the temperature for both samples. One can see that the B_{max} decreases as the temperature increases for both samples. This can be attributed to the reduced influence of spin freezing since it becomes easier for spin rotation at a higher temperature under the external magnetic field.

For all samples except for the H2 141-nm sample, $(\rho^T_{xy})_{max}$ slightly increases with temperature. The THE will eventually be overwhelmed by thermal fluctuations at high enough temperatures. Therefore, the maximum of THE for these samples should be at elevated temperatures above 300 K. In contrast, the maximum for the H2 141-nm sample is below 50 K (Figure S5, Supporting Information). However, the intensity of THE is also affected by the exchange interaction and the magnetic anisotropy, which are controlled by the sample composition and the film thickness, respectively, and the intensity of THE for H1 and H2 samples is not sensitive to the change of temperature. Therefore, the thermal activation of THE could not be manifested in the thermal dependence. To verify the thermal activation process of the THE, we performed the first principles density functional theory (DFT) calculations at $T = 0$ K and Monte Carlo (MC) simulations at finite temperatures, respectively. The DFT calculations showed that the spin configuration of the FCNM CCA system at $T = 0$ K is collinear, indicating that the spin chirality is suppressed under this condition.[34] Therefore, it appears that a thermal perturbation is a necessary condition for the formation of THE. When the temperature surpasses a critical value, the long-range magnetic order is eliminated by thermal fluctuations, and the sample becomes paramagnetic. This transition can lead to the disappearance of spin chirality and THE.

We conducted MC simulations to investigate the effect of thermal fluctuations on the formation of THE. Due to the vast complexity of CCAs, including the slightly distorted fcc lattice and the random occupation of magnetic atoms, it is extremely challenging to reproduce the realistic experimental circumstances in MC simulations. In previous studies, simplified 2D spin lattice models were used to investigate the noncoplanar magnetism in bulk materials.[43,44] Therefore, we utilized a 2D model system to replicate the characteristics of the FCNM CCA. A representative MC simulation illustrates that the variation of topological charge Q (proportional to the total THE of the system)[45,46] versus the magnetic field (Figure S6, Supporting Information) is consistent with the results shown in Figure 2d. To probe the thermal dependence of the THE, MC simulations in systems with various strength of exchange interactions were conducted. The results show that the THE typically exhibits a thermally activated characteristic (Figure S7a–d, Supporting Information). For systems with stronger ferromagnetism, the temperature for the maximum THE becomes higher, indicating that it is harder to activate the noncoplanar magnetism by thermal fluctuations. Considering that the intensity of THE is not sensitive to the temperature, the broad experimental temperature range of 50–300 K should correspond to a narrow simulational range. Therefore, a different thermal dependence of THE could be observed within a fixed temperature range for samples with different compositions. Furthermore, the magnetic shape anisotropy controlled by film thickness can also significantly change the thermal dependence of THE (Figure S7e–i, Supporting Information). These results demonstrate that THE is

thermally activated and can be drastically altered by tuning the composition and the thickness of the samples, which accounts for the discrepancy of thermal dependence experimentally observed in the H1 and H2 samples (Figure S5, Supporting Information).

Conventional ferromagnetic metals typically exhibit a negative correlation between MR and external field at room temperature.[47] However, for the FCNM CCA films, the MR (Figure S4, Supporting Information) shows a broad hump atop the linear component. The high-field negative correlation is indicative of the reduced magnetic scattering on the itinerant electrons. Yet, it should be noted that the magnitude of the critical magnetic field at the maximal THE and MR are different, for example, it is ≈0.2 T for THE but always 0.5 T for MR (in the H1 81-nm sample). The thermal dependence of MR and the THE is also inconsistent, for example, the MR shows a much larger thermal dependence than that of the THE (in the 1.9-μm sample). Therefore, the anomalies in MR cannot be simply attributed to the influence of chiral spin structures and deserve further experimental and theoretical investigations.

At 300 K, the 81-nm sample exhibits a maximum THE of 1.92 μΩ cm. The intensity is significantly higher than that of typical magnetic skyrmion systems like MnSi (4.5 nΩ cm in bulk samples and 10 nΩ cm in epitaxial thin films),[18,48] NiMnGa (150 nΩ cm in bulk samples and 135 nΩ cm in films),[42,49] and FeGe (5 nΩ cm in bulk forms and 160 nΩ cm in epitaxial films).[50,51] This indicates an exceptionally dense population of CSTs in the FCNM CCA films. Moreover, the abundant presence of CSTs in the FCNM thin films suggests that their sizes may be much smaller than those of magnetic skyrmions, perhaps down to the atomic scale. For skyrmion systems, the effective magnetic flux density B_{eff} and the skyrmion density n_{sk} can be estimated by $\rho^T_{xy} = PR_0B_{eff} = PR_0n_{sk}\Phi_0$, where P is the transport spin polarization, R_0 is the effective charge density usually taken as the ordinary Hall coefficient, and Φ_0 is the magnetic flux quantum.[35] Assuming that the spins are completely polarized, then the value of $(\rho^T_{xy})_{max}$ (1.92 μΩ cm) for the H1 sample corresponds to a $B_{eff} \approx 60.7$ T and a $n_{sk} \approx 0.03/nm^2$. The n_{sk} for H1 is much higher than that reported in typical magnetic skyrmion systems.[52] The topological transport properties for the H2 sample are also shown in Figure S5, Supporting Information. The maximum intensity of THE for H2 reaches 1.48 μΩ cm, which is lower than that of H1. The reduced intensity of THE in H2 can be attributed to the difference in the chemical composition between H1 and H2. Considering that the grain sizes of H1 and H2 samples are significantly different, there should be a substantial divergence in the spatial density of grain boundaries. However, their maximum intensity of THE is comparable, which indicates it is next to impossible that the grain boundary is the source of the spin chirality. Furthermore, the grain boundaries have not yet been reported as a formation mechanism of noncoplanar magnetism so far.[35]

2.3. Micromagnetic Characterization

To gain a deeper insight into the underlying mechanism of the THE in the FCNM CCA films, we conducted a Lorentz-TEM (L-TEM) investigation of the magnetic domain structures and their response to the external magnetic field. **Figure 3b** depicts the

**ADVANCED
SCIENCE NEWS**

www.advancedsciencenews.com
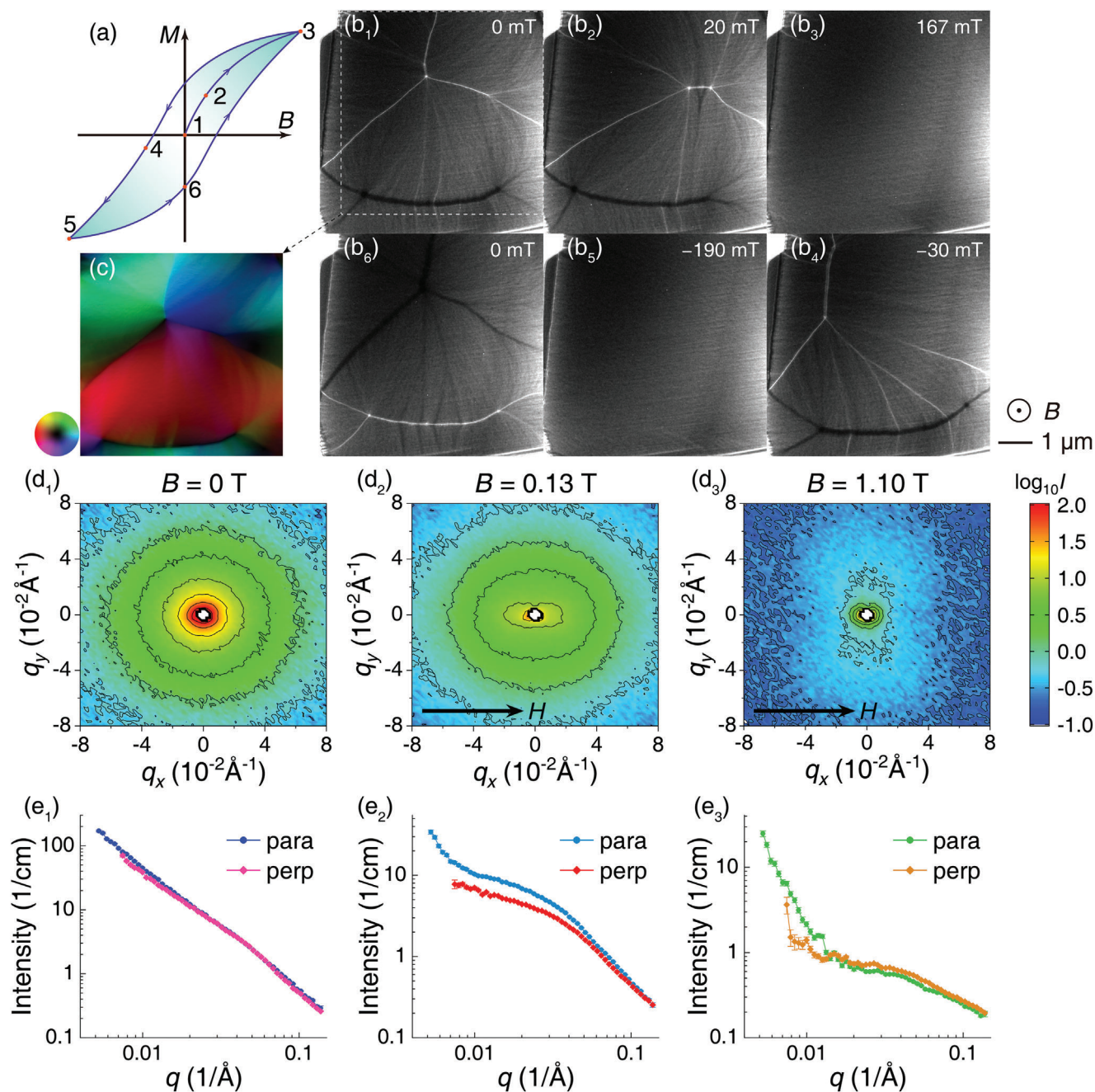
**ADVANCED
MATERIALS**

www.advmat.de

Figure 3. L-TEM and SANS results for H1. a) Evolution of the applied fields for the L-TEM experiments. b) Real space observation of magnetic domain walls for the H1 sample. c) Distribution of spins calculated by TIE for the area marked in (a₁). d) Scanning maps of SANS results under various applied fields. e) Azimuthal integrals of the scattering data along (para) and perpendicular to (perp) the direction of the applied field.

evolution of magnetic domain walls with respect to the applied magnetic field (Figure 3a) for the H1 sample. As the sample is soft ferromagnetic (Figure S8, Supporting Information), we initially demagnetized the sample before the experiment. The L-TEM image at zero field (Figure 3b$_1$) clearly reveals the presence of a Landau-domain pattern at the top and cross-tie walls at the bottom. Figure 3c depicts the corresponding spin orientation, which is computed using the transport-of-intensity equations (TIE). Interestingly, the spin configuration is smooth and

devoid of short-wavelength spin modulation. Except for the major domain walls with sharp contrast, there are some minor domain walls that have lower thickness and contrast. The angle of spins on either side of the minor walls is smaller, indicating that the spin configuration inside each domain is noncollinear. When an out-of-plane magnetic field was applied, the walls began to move and the Landau domain split into two separate parts (Figure 3b$_2$). Upon increasing the external field to 167 mT, the walls completely disappeared, resulting in the merger into a sin-

gle domain (Figure 3b$_3$). Once turning off the field, the walls of the domains returned to their initial state. Subsequently, a magnetic field with a reversed direction was applied, causing the walls to vanish again at a field strength of 190 mT (Figure 3b$_5$). The behavior of the walls during the gradual switch-off of the reversed field is analogous, and as a result, the contrast of the final L-TEM image at zero field (Figure 3b$_6$) is inverted compared with the initial one. The evolution of domain walls for the H2 sample exhibits a comparable behavior, as depicted in Figure S9, Supporting Information. While cross-tie domain walls consist of alternating chains of magnetic vortices and anti-vortices with a topological charge of $\pm 1/2$, the estimated density of vortices in Figure 3a is far less than $1/\mu m^2$, which is not consistent with the value estimated from the intensity of the THE. Besides, at $B = 167$ mT, the intensity of THE for the 81-nm H1 sample is ≈ 1.88 $\mu\Omega$ cm, despite the fact that the vortices have already disappeared in the L-TEM image. This evidence suggests that domain walls and magnetic vortices observed in L-TEM cannot explain the origin of THE.

To further investigate the chiral spin structures, SANS experiments were conducted on a bulk FCNM CCA sample, which has the same crystal structure and composition as the H1 film sample. The sample was subjected to transverse magnetic fields of 0, 0.13, and 1.1 T (Figure S10, Supporting Information) when the intensity of the resulting scattering was collected using a 2D detector (Figure 3d). To evaluate the contribution from spin misalignment, the scattering patterns were azimuthally integrated over narrow $-10°$–$10°$ regions along and perpendicular to the direction of the applied magnetic field, respectively (Figure 3e). At zero field, the scattering is particularly intensive in the range of q_x, $q_y < 0.08$/Å (Figure 3d$_1$), suggesting a glassy-like and disordered spin configuration. The azimuthal integrals are practically indistinguishable (Figure 3e$_1$), which indicate that the distribution of spin orientation is isotropic. The disordered distribution of spins can be attributed to severe magnetic frustration, which is caused by chemical disorder within the fcc lattice.[34] When a moderate transverse field of $B = 0.13$ T was applied, the intensity of neutron scattering caused by the magnetic moments became weaker due to the alignment of spins along the direction of B (Figure 3d$_2$). However, the nuclear scattering remained unchanged despite the application of the field. As a result, there was a slight difference in intensity between the transverse and longitudinal directions (Figure 3e$_2$). Although the spins possess a preferred orientation, they are still noncoplanar. Under an almost saturated magnetic field of $B = 1.10$ T (Figure S8, Supporting Information), the spins are almost entirely aligned, resulting in a significant decrease in the magnetic scattering while the nuclear scattering predominates (Figure 3d$_3$). The anisotropy becomes negligible as the sample is polycrystalline, and the structure is isotropic (Figure 3e$_3$). The significant difference between Figure 3d$_2$,d$_3$ suggests that despite the vanish of domain walls, the orientation of spins still exhibits an amorphous character when the magnitude of the THE reaches its maximum value. The SANS results indicate that the vector field of spins for the FCNM CCAs can be decomposed into two components: a ferromagnetic component aligning with the direction of the external field and a fully random component. The second term decreases as a function of the field and may be related to the spin chirality. Notably, despite being a soft ferromagnetic material, the spin

configuration of the H1 sample may remain noncoplanar even if it has become a single magnetic domain structure under the applied field.

2.4. The Mechanism of THE

Based on the combined results of L-TEM and SANS experiments and MC simulations, the formation mechanism of the THE can be proposed as follows, as illustrated in **Figure 4**: i) In the absence of an external field, the coexistence of ferromagnetic and antiferromagnetic exchange interactions results in a multi-domain structure, where the spins in each domain are noncoplanar. The chemical disorder of CCA implies a lack of preferential direction for the spin configuration. As a result, the total magnetization and spin chirality cancel out, leading to the observation of zero THE (Figure 4a). ii) Upon applying an external magnetic field, technical magnetization commences, and magnetic domains progressively merge into a single domain. The spins gradually align with the direction of the external field, leading to a reduction in the solid angle subtended by neighboring spins. However, despite the decrease in the magnitude of the spin chirality, the net spin chirality increases and becomes non-zero, which may result in the emergence of the THE (Figure 4b). iii) As the magnetic field is further increased, the spins become more aligned with the field direction, causing a decrease in the total spin chirality. During this stage, the intensity of the THE exhibits a negative correlation with the external field. iv) At the saturated field, the spins become fully aligned and collinear, resulting in the simultaneous disappearance of the spin chirality and the THE (Figure 4c). These evolutions of spin configurations can be well corroborated by MC simulations (Figure S6, Supporting Information).

3. Discussions

Earlier studies have revealed that the FCNM CCAs exhibit a reentrant spin glass behavior, with a glass transition temperature even above room temperature.[34] This observation implies a high degree of magnetic frustration in these alloys. The strong magnetic frustration arises from the direct short-range exchange interactions among the magnetic atoms situated on the close-packed lattice. We also performed temperature-dependent magnetization measurements on the FCNM thin films (Figure S11, Supporting Information). It can be clearly seen that the H1 film also exhibits a reentrant spin glass behavior with a freezing temperature of 15.4 K. The difference in freezing temperature of H1 with the bulk alloy can be attributed to the form of a film. This can serve as strong evidence for the presence of magnetic frustration in H1 samples and corroborate the glassy-like spin configuration observed by SANS experiments.

To further predict the magnetism of H1 and H2, we utilized DFT calculations on supercells consisting of 100 atoms, with due consideration to the SOC effect. The results are shown in Figure S12, Supporting Information. It can be found that the magnetic moment characteristics are retained even if the Fe, Co, and Ni atoms are no longer in equiatomic proportions.[34,53] Furthermore, a minor energy shift of less than 5×10^{-4} meV/atom

**ADVANCED
SCIENCE NEWS**

www.advancedsciencenews.com

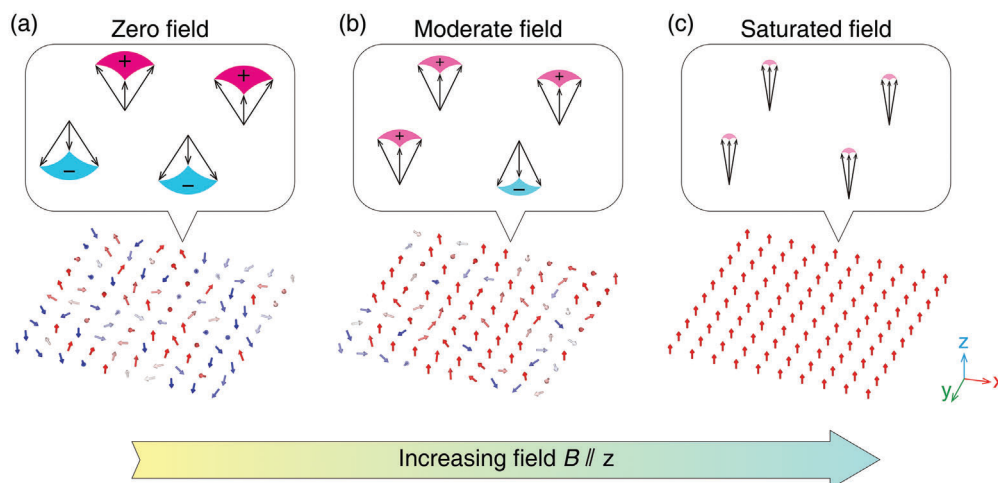**ADVANCED
MATERIALS**

www.advmat.de

Figure 4. Noncoplanar magnetism of FCNM CCAs. Schematic diagram of spin chirality and configuration at zero field (a), moderate field (b), and saturated field (c).

is observed upon switching the direction of the magnetic field, suggesting that the magnetocrystalline anisotropy is negligible. This result excludes magnetocrystalline anisotropy as the source of noncoplanar magnetism.

THE induced by geometric frustration in magnets has been reported in studies of materials such as Gd_2PdSi_3[27] and $Gd_3Ru_4Al_{12}$.[28] In these systems, magnetic frustration arises due to the oscillatory nature of the RKKY interaction between neighboring $4f$ moments. In contrast, the dominant magnetic interaction in FCNM CCAs is governed by the Heisenberg exchange coupling, which has a substantially higher strength than the RKKY interaction owing to its short-range nature. Given that all atoms in FCNM CCAs are either ferromagnetic or antiferromagnetic, the level of magnetic frustration is significantly greater than that in conventional frustrated magnets, which often comprise a higher proportion of nonmagnetic atoms. Furthermore, this large degree of magnetic frustration in FCNM alloys can lead to the emergence of noncoplanar magnetism, characterized by significant spin chirality and the emergence of THE. As a result, the random distribution of magnetic atoms on the lattice sites, which is associated with the high-entropy effect in CCAs, presents a novel mechanism for inducing magnetic frustration and a new pathway for introducing spin chirality. Furthermore, the spin glass transition has also been observed in the CrMnFeCoNi high entropy alloy (known as Cantor alloy),[54] indicating that there exists magnetic frustration in the alloy. The observation of THE is also possible in the Cantor alloy.

In addition, the short-range nature of the exchange interaction between magnetic moments in FCNM CCAs is anticipated to result in smaller chiral spin structures, possibly with a size of only a few atoms, as compared to the long-range RKKY interaction in geometrically frustrated magnets. The size is much smaller than that observed in geometrically frustrated magnets (2.5 nm in Gd_2PdSi_3 and 2.8 nm in $Gd_3Ru_4Al_{12}$). This attribute positions FCNM CCA films as promising candidates for the development of next-generation storage devices, with higher carrier density.

Although THE has long been thought to be associated with topological spin textures, such as skyrmions, [35] whose magnetic

domain walls can be visualized using L-TEM, the striking THE observed in FCNM CCAs appears to be unrelated to these walls. This is primarily because the underlying mechanism of spin chirality does not rely on the existence or the topological nature of walls. Hence, the correlation between the size of skyrmions and the intensity of THE is not universal and applies only to specific skyrmion systems. As supporting evidence, the maximum amplitudes of THE in MnGe, MnSi, and $Mn_{1.4}PtSn$ are 0.16, 4.5, and 1.53 $\mu\Omega$ cm, respectively, despite having skyrmion sizes of 3, 18, and 150 nm.[55–57] This discrepancy highlights the reason why remarkable THE can be observed in FCNM CCA films, even in the absence of high-density topological domain walls. Furthermore, in skyrmion systems, the noncoplanar magnetism and spin chirality are usually attributed to the DM interaction. It stems from the SOC, which is a relativistic correction to the magnetism. However, given the difference in strength between the direct exchange coupling and the effect of DM interaction, which only perturbs collinear magnetism, the THE observed in skyrmion systems is generally weaker than that observed in FCNM CCAs, where the spin chirality is favored by the applied magnetic field.

4. Conclusions

To conclude, we have observed a prominent THE (1.92 $\mu\Omega$ cm) in ion-beam-deposited FCNM CCA films. These films exhibit a single-phase solid solution with an fcc crystal structure, and the THE remains observable across a broad range of temperatures and applied magnetic fields. The underlying physics of the THE is distinct from skyrmion systems, as well as geometrically frustrated magnets reported thus far. Notably, the spin chirality in FCNM CCAs stems from the strong magnetic frustration and is favored by the application of external magnetic fields. The magnetic frustration in FCNM CCA can be ascribed to the random occupation of magnetic elements on the fcc lattice, which establishes competing direct exchange interactions and gives rise to noncoplanar magnetism. Furthermore, the chemical disorder in FCNM CCAs offers precise control over the modulation of magnetic frustration by adjusting the stoichiometry composition,

thereby enabling the development of systems with specific degrees of spin chirality. In this sense, FCNM CCAs represent a promising platform for the investigation of CSTs, as well as potential applications in the field of spintronic devices.

5. Experimental Section

Sample Preparation: H1 and H2 samples were fabricated by ion beam deposition with the powder-sintered target (PST) and the induction melted target (IMT), respectively. The IMT was synthesized by induction melting pure Mn, Fe, Co, and Ni metals into an alloy ingot and casting it into the disk shape. The PST was made by grinding the element powders, pressing mixed powder into the desired shape, and sintering it into a target. The nominal composition of both targets was FeCoNiMn 1:1:1:1 in atomic ratio. Since the PST was sintered below the melting point of the alloy, its elemental homogeneity was worse than the IMT. Samples for various measurements were grown on different substrates simultaneously: a single crystal Si substrate of 2 in. in diameter for microstructure characterizations and film thickness measurements; a bar shape Si substrate about 1 × 3 mm in size for magnetization measurements; a silicate glass substrate for electrical transport measurements. The background vacuum was 4 × 10^{-4} Pa, and the working pressure was 2.4 × 10^{-2} Pa. The acceleration voltage was 750 V and the beam current of Ar^+ ion was 60 mA.

Structural Characterizations: Crystal structures of samples were characterized by grazing incident X-ray diffraction (Bruker D8 Advance). The GI-XRD scanning was repeated several times to obtain a better result with a higher signal-to-noise ratio. The film thickness was determined using XRR (Bruker D8 Advance) for samples under 200 nm in thickness, and SEM observation of cross-section (Thermo-Fisher Scientific Quattro S) for samples above 800 nm. The composition of films was checked by EDS (Bruker XFlash 6|30).

TEM samples were prepared by lift-outs and thinned on an FEI Scios 2 focused ion beam/SEM (FIB/SEM). TEM experiments were conducted in an aberration-corrected Thermo-Fisher Scientific Titan Cubed Themis Z 60–300 equipped with an X-FEG gun and a Bruker Super-X EDS detector, operated at 300 kV with the beam current 50 pA. The scanning TEM (STEM) images and EDS mapping were acquired in a convergence semi-angle of 21.5 mrad, and a collection semi-angle snap of 80–379 mrad.

Transport Property Measurements: Electrical transport measurements under cryogenic temperatures were performed by a physical property measurement system (Quantum Design). A stainless-steel mask was used to get film samples in a Hall bar shape. Contacts were made by platinum wires with silver paste in a standard four-probe configuration. Due to the inevitable misalignment of electrodes, the longitudinal resistance component in the Hall resistance was removed by scanning the magnetic field reversely and extracting the odd symmetric component. The OHE component can be extracted by a linear fit to the high-field region.

Magnetic Property Measurements: The magnetization measurements were conducted using a superconducting quantum interference device vibrating sample magnetometer (Quantum Design MPMS). The directions of the applied magnetic fields in the magnetization and the resistance measurements were both perpendicular to the film plane, and the geometry of the samples was identical to the core part (without the leads) of the Hall bars used in the transport property measurements. The paramagnetic component of the magnetization for the samples, as well as the diamagnetic component for the Si substrate, can be extracted together by linear fit to the high field region of the raw magnetic hysteresis loop.

L-TEM experiments were conducted on a Thermo-Fisher Scientific Titan G2 80–300 objective-lens aberration-corrected environmental TEM instrument operating at 300 kV. The real space observation of magnetic domain walls was performed by shutting down the objective lens.

SANS Experiments: The sample for the SANS experiments was prepared by arc-melting pure metals into alloy ingots under a Ti-gettered Ar atmosphere. During melting, each ingot was flipped and re-melted at least four times to guarantee the homogeneity of compositions. An excess of Mn (≈3% of its normal content) was added to compensate for the melt-ing loss owing to its vaporization. After arc-melting, the ingots were further encapsulated in a quartz tube and homogenized at 1373 K for 48 h, then water-quenched. Finally, disk-shaped samples of 15 mm in diameter and 1 mm in thickness were cut from the ingots using spark-erosion wire cutting. In order to get rid of the oxides, the surfaces of the samples were further polished into a bright finish.

The SANS was performed at China Spallation Neutron Source[58] (CSNS). The incident neutrons with wavelengths of 1–10 Å were defined by a double-disc bandwidth chopper, which was collimated to the sample by a pair of apertures. The experiment used the sample-to-detector distance of 4 m and a sample aperture of 6 mm. The 1 m square detector array was composed of 120 linear He-3 gas tubes with a diameter of 8 mm, which covered the Q-range between 0.01 and 1 $Å^{-1}$. The presented data correspond to ≈120 min of data collection time for each sample (@100 kW). Neutron data were corrected for background scattering (empty sample holder), transmission, and detector efficiency, and set to absolute units.

First Principles Calculations: The total energy at zero temperature was calculated using the Vienna Ab initio Simulation Package (VASP). The supercells of 100-atom fcc structures were generated through special quasi-random structures (SQS)[59] to model the random distribution using the Alloy Theoretic Automated Toolkit (ATAT) package developed by Axel van de Walle and his co-workers.[60,61] The projector augmented wave (PAW)[62] pseudopotentials and the generalized gradient approximation parametrized by Perdew, Burke, and Ernzerhof (PBE)[63] were used. A smearing parameter[64] of 0.2 eV and a plane-wave energy cutoff of 450 eV were chosen. The structure was optimized in a non-magnetic state first. Both the lattice parameter and the atomic coordinates were fully relaxed under zero pressure using the Monkhorst-Pack k-point meshes[65] of 3 × 3 × 3 until the energy convergence reached 1 meV/atom. Then a self-consistent calculation with collinear magnetism was performed. Finally, non-selfconsistent calculations with non-collinear magnetism and SOC were performed by reading in the output (including the wavefunction and the charge density) of the collinear calculation.

Monte Carlo Simulations: MC simulations were performed on systems that contained $N^2 = 32 \times 32$ spins with periodic boundary conditions and allowed 3D rotations of spins. The details about methods, including the Hamiltonian of the system and the Metropolis algorithm for the simulations, are described in previous articles.[45,46] The magnetic field was swept from −2 to 2 J and then back to −2 J with a step length of 0.01 J for every simulation, which covered the saturated magnetic field, and 10^4 MC steps were performed at each magnetic field step. The topological charge Q can be calculated, which is defined as the sum of spin chirality around the whole system and is proportional to the total THE of the system. Two parameters J_{EX} and J_{EA} were used to adjust the strength of the magnetic exchange correlation and the magnetic shape anisotropy of the system. J_{EX} can reflect the degree of ferromagnetism, which is manifested as differences in the saturated field and magnetization. J_{EA} can quantify the effect of the demagnetizing factor, where EA represents the easy axis. These parameters were all chosen to cover the entire reasonable range so that the resulting systems match the magnetic properties of the FCNM CCA samples. Specifically, the range of J_{EX} was chosen so that the system was neither hard ferromagnetic (too high) nor paramagnetic (too low); the upper limit of J_{EA} was below the critical value at which the exchange bias effects will emerge.

Supporting Information

Supporting Information is available from the Wiley Online Library or from the author.

Acknowledgements

Conflict of Interest

The authors declare no conflict of interest

Author Contributions

W.W., H.B., B.S., and Z.L. conceived the project. J.Y. prepared the materials and samples, and carried out the main experiments, first-principles calculations, and Monte Carlo simulations. Y.L. and J.S. conducted the TEM experiments. Y.K. conducted the SANS experiments. All authors participated in the discussions. J.Y. and B.S. wrote the manuscript, which was commented on by H.B., Y.K., and W.W.

Data Availability Statement

The data that support the findings of this study are available from the corresponding author upon reasonable request.

Keywords

[1] Y. Taguchi, Y. Oohara, H. Yoshizawa, N. Nagaosa, Y. Tokura, *Science* **2001**, *291*, 2573.
[2] S. Mühlbauer, B. Binz, F. Jonietz, C. Pfleiderer, A. Rosch, A. Neubauer, R. Georgii, P. Böni, *Science* **2009**, *323*, 915.
[3] L. Balents, *Nature* **2010**, *464*, 199.
[4] E. Skoropata, J. Nichols, J. M. Ok, R. V. Chopdekar, E. S. Choi, A. Rastogi, C. Sohn, X. Gao, S. Yoon, T. Farmer, R. D. Desautels, Y. Choi, D. Haskel, J. W. Freeland, S. Okamoto, M. Brahlek, H. N. Lee, *Sci. Adv.* **2020**, *6*, eaaz3902.
[5] B. Göbel, I. Mertig, O. A. Tretiakov, *Phys. Rep.* **2021**, *895*, 1.
[6] Z. Fang, N. Nagaosa, K. S. Takahashi, A. Asamitsu, R. Mathieu, T. Ogasawara, H. Yamada, M. Kawasaki, Y. Tokura, K. Terakura, *Science* **2003**, *302*, 92.
[7] N. Nagaosa, X. Z. Yu, Y. Tokura, *Philos. Trans. R. Soc., A* **2012**, *370*, 5806.
[8] A. Fert, N. Reyren, V. Cros, *Nat. Rev. Mater.* **2017**, *2*, 17031.
[9] S. S. P. Parkin, M. Hayashi, L. Thomas, *Science* **2008**, *320*, 190.
[10] X. Zhang, M. Ezawa, Y. Zhou, *Sci. Rep.* **2015**, *5*, 9400.
[11] H. Kawamura, *Phys. Rev. Lett.* **1992**, *68*, 3785.
[12] H. Ishizuka, N. Nagaosa, *Sci. Adv.* **2018**, *4*, eaap9962.
[13] P. Bruno, V. K. Dugaev, M. Taillefumier, *Phys. Rev. Lett.* **2004**, *93*, 096806.
[14] K.-Y. Meng, A. S. Ahmed, M. Bacani, A.-O. Mandru, X. Zhao, N. Bagués, B. D. Esser, J. Flores, D. W. McComb, H. J. Hug, F. Yang, *Nano Lett.* **2019**, *19*, 3169.
[15] L. Wang, Q. Feng, Y. Kim, R. Kim, K. H. Lee, S. D. Pollard, Y. J. Shin, H. Zhou, W. Peng, D. Lee, W. Meng, H. Yang, J. H. Han, M. Kim, Q. Lu, T. W. Noh, *Nat. Mater.* **2018**, *17*, 1087.
[16] M. Raju, A. Yagil, A. Soumyanarayanan, A. K. C. Tan, A. Almoalem, F. Ma, O. M. Auslaender, C. Panagopoulos, *Nat. Commun.* **2019**, *10*, 696.
[17] D. Maccariello, W. Legrand, N. Reyren, K. Garcia, K. Bouzehouane, S. Collin, V. Cros, A. Fert, *Nat. Nanotechnol.* **2018**, *13*, 233.
[18] A. Neubauer, C. Pfleiderer, B. Binz, A. Rosch, R. Ritz, P. G. Niklowitz, P. Böni, *Phys. Rev. Lett.* **2009**, *102*, 186602.
[19] A. S. Ahmed, A. J. Lee, N. Bagués, B. A. McCullian, A. M. A. Thabt, A. Perrine, P.-K. Wu, J. R. Rowland, M. Randeria, P. C. Hammel, D. W. McComb, F. Yang, *Nano Lett.* **2019**, *19*, 5683.
[20] Q. Shao, Y. Liu, G. Yu, S. K. Kim, X. Che, C. Tang, Q. L. He, Y. Tserkovnyak, J. Shi, K. L. Wang, *Nat. Electron.* **2019**, *2*, 182.
[21] Y. Cheng, S. Yu, M. Zhu, J. Hwang, F. Yang, *Phys. Rev. Lett.* **2019**, *123*, 237206.
[22] J. Matsuno, N. Ogawa, K. Yasuda, F. Kagawa, W. Koshibae, N. Nagaosa, Y. Tokura, M. Kawasaki, *Sci. Adv.* **2016**, *2*, e1600304.
[23] C. Moreau-Luchaire, C. Moutafis, N. Reyren, J. Sampaio, C. A. F. Vaz, N. Van Horne, K. Bouzehouane, K. Garcia, C. Deranlot, P. Warnicke, P. Wohlhüter, J.-M. George, M. Weigand, J. Raabe, V. Cros, A. Fert, *Nat. Nanotechnol.* **2016**, *11*, 444.
[24] S. Woo, K. Litzius, B. Krüger, M.-Y. Im, L. Caretta, K. Richter, M. Mann, A. Krone, R. M. Reeve, M. Weigand, P. Agrawal, I. Lemesh, M.-A. Mawass, P. Fischer, M. Kläui, G. S. D. Beach, *Nat. Mater.* **2016**, *15*, 501.
[25] O. Boulle, J. Vogel, H. Yang, S. Pizzini, D. de Souza Chaves, A. Locatelli, T. O. Mentes, A. Sala, L. D. Buda-Prejbeanu, O. Klein, M. Belmeguenai, Y. Roussigné, A. Stashkevich, S. M. Chérif, L. Aballe, M. Foerster, M. Chshiev, S. Auffret, I. M. Miron, G. Gaudin, *Nat. Nanotechnol.* **2016**, *11*, 449.
[26] T. Moriya, *Phys. Rev.* **1960**, *120*, 91.
[27] T. Kurumaji, T. Nakajima, M. Hirschberger, A. Kikkawa, Y. Yamasaki, H. Sagayama, H. Nakao, Y. Taguchi, T.-H. Arima, Y. Tokura, *Science* **2019**, *365*, 914.
[28] M. Hirschberger, T. Nakajima, S. Gao, L. Peng, A. Kikkawa, T. Kurumaji, M. Kriener, Y. Yamasaki, H. Sagayama, H. Nakao, K. Ohishi, K. Kakurai, Y. Taguchi, X. Yu, T.-H. Arima, Y. Tokura, *Nat. Commun.* **2019**, *10*, 5831.
[29] N. D. Khanh, T. Nakajima, X. Yu, S. Gao, K. Shibata, M. Hirschberger, Y. Yamasaki, H. Sagayama, H. Nakao, L. Peng, K. Nakajima, R. Takagi, T.-H. Arima, Y. Tokura, S. Seki, *Nat. Nanotechnol.* **2020**, *15*, 444.
[30] D. Grohol, K. Matan, J.-H. Cho, S.-H. Lee, J. W. Lynn, D. G. Nocera, Y. S. Lee, *Nat. Mater.* **2005**, *4*, 323.
[31] M. A. Ruderman, C. Kittel, *Phys. Rev.* **1954**, *96*, 99.
[32] T. Kasuya, *Prog. Theor. Phys.* **1956**, *16*, 45.
[33] K. Yosida, *Phys. Rev.* **1957**, *106*, 893.
[34] J. Yu, W. Wu, H. Zhang, R. Shao, F. Zhang, H. Wang, Z. Li, J. Luan, Z. Jiao, C. T. Liu, B. Sun, H. Bai, W. Wang, *Phys. Rev. Mater.* **2022**, *6*, L091401.
[35] H. Wang, Y. Dai, G.-M. Chow, J. Chen, *Prog. Mater. Sci.* **2022**, *130*, 100971.
[36] G. Kimbell, C. Kim, W. Wu, M. Cuoco, J. W. A. Robinson, *Commun. Mater.* **2022**, *3*, 19.
[37] W. Zhang, P. K. Liaw, Y. Zhang, *Sci. China Mater.* **2018**, *61*, 2.
[38] E. P. George, D. Raabe, R. O. Ritchie, *Nat. Rev. Mater.* **2019**, *4*, 515.
[39] M.-H. Tsai, J.-W. Yeh, *Mater. Res. Lett.* **2014**, *2*, 107.
[40] L. Han, F. Maccari, I. R. Souza Filho, N. J. Peter, Y. Wei, B. Gault, O. Gutfleisch, Z. Li, D. Raabe, *Nature* **2022**, *608*, 310.

[41] Q. F. He, J. G. Wang, H. A. Chen, Z. Y. Ding, Z. Q. Zhou, L. H. Xiong, J. H. Luan, J. M. Pelletier, J. C. Qiao, Q. Wang, L. L. Fan, Y. Ren, Q. S. Zeng, C. T. Liu, C. W. Pao, D. J. Srolovitz, Y. Yang, *Nature* **2022**, *602*, 251.

[42] B. Ding, Y. Li, G. Xu, Y. Wang, Z. Hou, E. Liu, Z. Liu, G. Wu, W. Wang, *Appl. Phys. Lett.* **2017**, *110*, 092404.

[43] X. Z. Yu, Y. Onose, N. Kanazawa, J. H. Park, J. H. Han, Y. Matsui, N. Nagaosa, Y. Tokura, *Nature* **2010**, *465*, 901.

[44] S. Pöllath, J. Wild, L. Heinen, T. N. G. Meier, M. Kronseder, L. Tutsch, A. Bauer, H. Berger, C. Pfleiderer, J. Zweck, A. Rosch, C. H. Back, *Phys. Rev. Lett.* **2017**, *118*, 207205.

[45] W. Wang, M. W. Daniels, Z. Liao, Y. Zhao, J. Wang, G. Koster, G. Rijnders, C.-Z. Chang, D. Xiao, W. Wu, *Nat. Mater.* **2019**, *18*, 1054.

[46] W. Wang, Y.-F. Zhao, F. Wang, M. W. Daniels, C.-Z. Chang, J. Zang, D. Xiao, W. Wu, *Nano Lett.* **2021**, *21*, 1108.

[47] T. McGuire, R. Potter, *IEEE Trans. Magn.* **1975**, *11*, 1018.

[48] Y. Li, N. Kanazawa, X. Z. Yu, A. Tsukazaki, M. Kawasaki, M. Ichikawa, X. F. Jin, F. Kagawa, Y. Tokura, *Phys. Rev. Lett.* **2013**, *110*, 117202.

[49] W. Wang, Y. Zhang, G. Xu, L. Peng, B. Ding, Y. Wang, Z. Hou, X. Zhang, X. Li, E. Liu, S. Wang, J. Cai, F. Wang, J. Li, F. Hu, G. Wu, B. Shen, X.-X. Zhang, *Adv. Mater.* **2016**, *28*, 6887.

[50] M. Leroux, M. J. Stolt, S. Jin, D. V. Pete, C. Reichhardt, B. Maiorov, *Sci. Rep.* **2018**, *8*, 15510.

[51] S. X. Huang, C. L. Chien, *Phys. Rev. Lett.* **2012**, *108*, 267201.

[52] Y. Tokura, N. Kanazawa, *Chem. Rev.* **2021**, *121*, 2857.

[53] T. Zuo, M. C. Gao, L. Ouyang, X. Yang, Y. Cheng, R. Feng, S. Chen, P. K. Liaw, J. A. Hawk, Y. Zhang, *Acta Mater.* **2017**, *130*, 10.

[54] O. Schneeweiss, M. Friák, M. Dudová, D. Holec, M. Sob, D. Kriegner, V. Holý, P. Beran, E. P. George, J. Neugebauer, A. Dlouhý, *Phys. Rev. B* **2017**, *96*, 014437.

[55] N. Kanazawa, Y. Onose, T. Arima, D. Okuyama, K. Ohoyama, S. Wakimoto, K. Kakurai, S. Ishiwata, Y. Tokura, *Phys. Rev. Lett.* **2011**, *106*, 156603.

[56] A. Tonomura, X. Yu, K. Yanagisawa, T. Matsuda, Y. Onose, N. Kanazawa, H. S. Park, Y. Tokura, *Nano Lett.* **2012**, *12*, 1673.

[57] A. K. Nayak, V. Kumar, T. Ma, P. Werner, E. Pippel, R. Sahoo, F. Damay, U. K. RoBler, C. Felser, S. S. P. Parkin, *Nature* **2017**, *548*, 561.

[58] Y. Ke, C. He, H. Zheng, Y. Geng, J. Fu, S. Zhang, H. Hu, S. Wang, B. Zhou, F. Wang, J. Tao, *J. Neutron Res.* **2018**, *29*, 14.

[59] A. Zunger, S. H. Wei, L. G. Ferreira, J. E. Bernard, *Phys. Rev. Lett.* **1990**, *65*, 353.

[60] A. van de Walle, P. Tiwary, M. de Jong, D. L. Olmsted, M. Asta, A. Dick, D. Shin, Y. Wang, L.-Q. Chen, Z.-K. Liu, *Calphad* **2013**, *42*, 13.

[61] A. van de Walle, *Calphad* **2009**, *33*, 266.

[62] G. Kresse, D. Joubert, *Phys. Rev. B* **1999**, *59*, 1758.

[63] J. P. Perdew, K. Burke, M. Ernzerhof, *Phys. Rev. Lett.* **1996**, *77*, 3865.

[64] M. Methfessel, A. T. Paxton, *Phys. Rev. B* **1989**, *40*, 3616.

[65] H. J. Monkhorst, J. D. Pack, *Phys. Rev. B* **1976**, *13*, 5188.